Research Article Vol. 32, No. 12 / 3 Jun 2024 / Optics Express 21134
Optics EXPRESS

Three-dimensional detection of CO_2 and wind using a 1.57 μm coherent differential absorption lidar

SAIFEN YU,[1,2] KEXIN GUO,[1] SHENGHAO LI,[1] HAOBIN HAN,[1] ZHEN ZHANG,[1,2,4] AND HAIYUN XIA[1,3,5]

[1]School of Atmospheric Physics, Nanjing University of Information Science and Technology, Nanjing 210044, China
[2]National Center of Carbon Metrology (Fujian), Nanping 353011, China
[3]School of Earth and Space Science, University of Science and Technology of China, Hefei 230026, China
[4]003514@nuist.edu.cn
[5]hsia@ustc.edu.cn

Abstract: A 1.57-μm coherent differential absorption lidar is demonstrated for measuring three-dimensional CO_2 and wind fields simultaneously. The maximum detection range of CO_2 is up to 6 km with a range resolution of 120 m and a time resolution of 1 min. A preliminary assessment of instrument performance is made with a 1-week continuous observation. The CO_2 concentration over a column from 1920 to 2040 m is compared with the one measured by an optical cavity ring-down spectrometer placed on a 2 km-away meteorological tower. The concentration is strongly correlated with the in-situ spectrometer with a correlation coefficient and RMSE of 0.91 and 5.24 ppm. The measurement accuracy of CO_2 is specified with a mean and standard deviation of 2.05 ppm and 7.18 ppm, respectively. The regional CO_2 concentration and the three-dimensional wind fields are obtained through different scanning modes. Further analysis is conducted on vertical mixing and horizontal transport of CO_2 by combining with the measured wind fields.

1. Introduction

Greenhouse gases, mainly carbon dioxide (CO_2), strongly absorb infrared long wave radiation emitted by the ground and air, playing a key role in global climate change [1–3]. The accumulation of CO_2 concentration over the years is increasing due to its long lifetime of 100-200 years. In the pre-industrial period, the CO_2 concentration remained at 278 ppm but has grown to 418 ppm in 2022, with an increase of 150% [4]. The spatial and temporal distribution of CO_2 is variable and the knowledge of the sources and sinks of CO_2 is still inadequate [5–7]. Range-resolved differential absorption lidar (DIAL) has been established for remotely sensing atmospheric CO_2 [8–11]. Recently, the superconducting nanowire single photon detector (SNSPD) has been investigated and developed for direct detection DIAL with high sensitivity and signal-to-noise ratio (SNR) but added complexity and cost [12,13]. Instead, the coherent detection technique is characterized by improved receiving sensitivity and suppressed solar background noise, which overcomes the detector issue. The quality of coherent DIAL signals is often expressed by the carrier-to-noise ratio (CNR) rather than the SNR expressed in the direct detection [14–16]. Scanning coherent Doppler lidar is demonstrated for remotely sensing air pollutants with range resolution [17,18]. The requirement of pulse power is several orders of magnitude smaller than that in the conventional direct detection technique. Besides, the detector current of coherent detection contains both amplitude and phase information. Thus, atmospheric CO_2 concentration and wind velocity can be measured simultaneously by combining the heterodyne technique and

#523904 https://doi.org/10.1364/OE.523904
Journal © 2024 Received 18 Mar 2024; revised 1 May 2024; accepted 15 May 2024; published 23 May 2024

Optics EXPRESS

differential absorption technique [19], which contributes to further studying CO_2 horizontal transport and vertical flux [20,21].

Researches on atmospheric gases using coherent DIAL have been reported. A 10.6-μm pulsed coherent lidar is employed to measure water vapor profile and radial velocity, which illustrates the sensitivity advantage of heterodyne detection [22]. Subsequently, the detection wavelength moves to near-infrared of 1.5 μm region due to eye safety and the evolution of devices for optical fibers [23–26]. The 1.53-μm coherent DIAL is demonstrated for profiling water vapor and wind with a limited direction of the line of sight (LOS) measurement [27]. Besides, a fiber coherent DIAL at 1.65-μm is designed for remote sensing of methane leaks and wind [28]. Recent studies show that the wavelengths of coherent DIAL are mainly focused on 2-μm for simultaneously measuring CO_2 and wind [29–33]. Rare attempt has so far been made to apply the 1.5 μm coherent DIAL to CO_2 measurement due to weak absorption line intensity. And currently coherent DIALs lack multi-dimensional measurement and analysis on concentration and wind, which hinder the understanding of horizontal transport and vertical flux of CO_2 on various temporal and spatial scales.

In this work, an all-fiber, compact coherent DIAL at 1.57-μm is developed for simultaneously measuring horizontal and vertical CO_2 and wind fields. The performance of the coherent DIAL is further examined by a tower-based optical cavity ring-down spectrometer (CRDS). With the function of beam scanning, the three-dimensional (3-D) concentration and wind over a given area are obtained. The research would facilitate a detailed understanding of CO_2 spatiotemporal distribution, which helps to further analyze CO_2 sources and sinks on a regional scale. The next of this paper is structured as follows. In Section 2, the design and principle of the all-fiber scanning coherent DIAL are introduced. In Section 3, the 3-D atmospheric measurement results including comparison with in-situ sensor and systematic error are analyzed. Besides, the horizontal transport and vertical mixing process of CO_2, as well as the impacts of external and local emission sources on concentration distribution are further specified by combing with the measured wind data. Finally, the conclusion is summarized in Section 4.

2. System design and principle

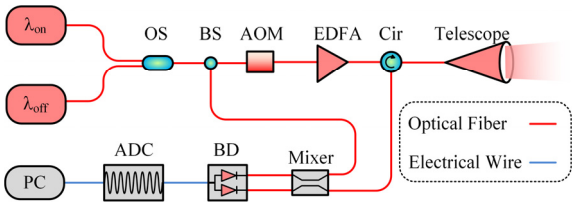

Fig. 1. System setup of CO_2 coherent DIAL. λ_{on}, on-line laser; λ_{off}, off-line laser; OS, optical switch; BS, beam splitter; AOM, acousto-optic modulator; EDFA, erbium-doped fiber amplifier; Cir, fiber circulator; BD, balanced detector; ADC, analog-to-digital converter; PC, personal computer.

The lidar is based on coherent Doppler and differential absorption techniques. As shown in Fig. 1, two seed lasers (Koheras MIKRO C15, NKT photonics) provide on-line and off-line emissions at 1572.335 nm and 1572.454 nm respectively. The lasers maintain good frequency stability due to precise temperature control. The frequency fluctuation in seconds and the frequency drift in hours are described in Table 1. In addition, the two wavelengths are calibrated monthly by a CO_2 cell for outdoor operation. The emissions are selected by an optical switch and pass through alternately using the time-division multiplexing technique. On the one hand, the selected output is chopped to pulse and shifted by 80 MHz using an acousto-optic modulator

Optics EXPRESS

(AOM) with a pulse duration of 800 ns and a pulse repetition frequency (PRF) of 10 kHz. Then, the output pulse is amplified by an erbium-doped optical fiber amplifier and is transmitted to the atmosphere through a 200-mm diameter telescope. The telescope can be pointed to any direction using a conical scan mechanism so that the output laser beam can be conically scanned for 3-D observation. On the other hand, a beam splitter is used to separate a part of the selected output for the local oscillator, which is mixed with the light collected by the telescope for heterodyne detection. The backscattered signal in each range bin is heterodyne-detected by a balanced detector (BD) and converted to the electrical signal. After analog-to-digital conversion, the detected signal at each bin is a beat note between the local oscillator and atmospheric scatter. The beat note is a frequency spectrum with its frequency indicating the Doppler-shifted frequency and with its amplitude relating to the power of the atmospheric scatter.

Table 1. Specifications of coherent DIAL

Parameters	Coherent DIAL
Wavelength	1572 nm
PRF	10 kHz
Pulse energy	80 μJ
Pulse width	800 ns
AOM shift	80 MHz
Frequency fluctuation in seconds	0.2 MHz
Frequency drift in hours	4 MHz
Seed laser linewidth	15 kHz
Amplified pulse linewidth	1.8 MHz
Optical switch cross talk	25 dB
Telescope diameter	200 mm
Detector type	Balanced detector
Transmitting efficiency	79.4%
Receiving efficiency	57.5%
Detector responsivity	1.2 A/W
Scanning mode	PPI, VAD
Function	Regional and vertical CO_2, 3-D wind
Range resolution	120 m
Time resolution of wind	1 s
Time resolution of CO_2	1 min

In order to improve detection probability, incoherent accumulation of 1×10^4 consecutive pulses over 1 s are performed with on-line and off-line pulse alternated. The on-line and off-line data are processed by separating the odd and even sequence of pulse. The sampled signal is divided into 122 range gates before calculating the spectra. Each gate includes 400 samples with overlap. The 6th range gate contains a strong signal that corresponds to the specular reflection from the output optics. Then the 512-point fast Fourier transform is performed to estimate the power spectrum. In fact, the output photocurrent $i(t)$ of BD contains signal current $i_s(t)$ and noise current $i_n(t)$. Thus, the accumulated spectrum is represented as $PSD(f,t) = S_s(f,t) + S_n(f,t)$. Considering that the atmospheric signals in the range gates before specular reflection are unavailable, analysis of the spectra in those range gates allows to determine and correct the background noise $S_n(f,t)$ [34]. The noise-corrected power spectrum of the backscattered signal is estimated by normalizing the data to the average noise power spectrum, eliminating the effects of system frequency response. Then, the $\mathrm{CNR}_{i=\mathrm{on,off}}$ and the signal power ($P_{i=\mathrm{on,off}}$) are calculated using the corrected power

Optics EXPRESS

spectrum based on the one-peak Gaussian fitting method (See Appendix for details). Specifically, the frequency content of off-line signal is used to measure LOS velocity v_{LOS} for its relatively small atmospheric attenuation, which is expressed as $v_{\mathrm{LOS}} = (f\text{-}\Delta f)\cdot\lambda_{\mathrm{off}}/2$, where f is the Doppler frequency shift for aerosols, $\Delta f = 80$ MHz is the frequency shift by AOM. The accuracy of radial velocity estimation is mainly determined by the value of $\mathrm{CNR}_{\mathrm{off}}$ [35].

In the DIAL calculation, the frequency offset of 80 MHz shifted by AOM is accounted for according to the CO_2 absorption spectrum from the HITRAN database [36]. The CO_2 absorption coefficient is determined by signal power using the DIAL equation [29]

$$\alpha_{CO_2} = \frac{1}{2\,(R_2 - R_1)} \ln\left[\frac{P_{\mathrm{on}}\,(R_1)\,P_{\mathrm{off}}\,(R_2)}{P_{\mathrm{on}}\,(R_2)\,P_{\mathrm{off}}\,(R_1)}\right], \tag{1}$$

where $R_{i\,=\,1,2,\ldots}$ are different ranges with the adjacent subscript representing a range bin. The CNR in coherent detection is expressed as $(P\text{-}P_B)/P_B$, where P_B is the noise signal power. Theoretical relative errors of on-line and off-line signals can be estimated as [32]

$$\frac{\mathrm{std}(P)}{P} = \frac{1}{SNR} = N^{-0.5}(2\Delta R/c\delta t)^{-0.5}\left(1 + \frac{1}{CNR}\right), \tag{2}$$

where N is the number of shots, a number of statistically independent shots have to be accumulated to obtain a small random error of the absorption coefficient. $\delta t = 800$ ns is the pulse duration. ΔR is the range resolution, here $\Delta R = c\delta t\,/2$ is 120 m, c is the speed of light. Due to the alternating emissions of on-line and off-line lasers, the cross-correlation coefficient $\rho(P_{\mathrm{on}}, P_{\mathrm{off}})$ between P_{on} and P_{off} should be considered in calculating the relative error of the absorption coefficient by [30]

$$\frac{\mathrm{std}(\alpha_{CO_2})}{\alpha_{CO_2}} = \frac{1}{2\alpha_{CO_2}\Delta R}\left[\frac{\mathrm{std}^2(P_{\mathrm{off}})}{P_{\mathrm{off}}^2} + \frac{\mathrm{std}^2(P_{\mathrm{on}})}{P_{\mathrm{on}}^2} - 2\rho(P_{\mathrm{on}}, P_{\mathrm{off}})\frac{\mathrm{std}(P_{\mathrm{on}})}{P_{\mathrm{on}}}\frac{\mathrm{std}(P_{\mathrm{off}})}{P_{\mathrm{off}}}\right]^{0.5}, \tag{3}$$

here $\rho(P_{\mathrm{on}}, P_{\mathrm{off}})$ is used to investigate the effect of atmospheric turbulence on measurement errors, which is given as [37,38]

$$\rho(P_{\mathrm{on}}, P_{\mathrm{off}}) = \frac{\mathrm{cov}(P_{\mathrm{on}}, P_{\mathrm{off}})}{\mathrm{std}(P_{\mathrm{on}})\cdot\mathrm{std}(P_{\mathrm{off}})}, \tag{4}$$

where $\mathrm{std}(P_{\mathrm{on}})$ and $\mathrm{std}(P_{\mathrm{off}})$ are the standard deviations of the normalized lidar signal, $\mathrm{cov}(P_{\mathrm{on}}, P_{\mathrm{off}})$ is the covariance of the signals. The CO_2 concentration as well as the dry air-mixing ratio $X_{\mathrm{CO_2}}$ and its standard deviation are obtained by [32]

$$X_{\mathrm{CO_2}} = \frac{\alpha_{\mathrm{CO_2}}}{WF} = \alpha_{\mathrm{CO_2}} kT\frac{1 + X_{\mathrm{H_2O}}}{p\Delta\sigma}, \tag{5}$$

$$\frac{\mathrm{std}(X_{\mathrm{CO_2}})}{X_{\mathrm{CO_2}}} = [\mathrm{var}(WF)/(WF)^2 + \mathrm{var}(\alpha_{\mathrm{CO_2}})/\alpha_{\mathrm{CO_2}}^2]^{-0.5}, \tag{6}$$

where WF is a weighting function of spectroscopic parameters and meteorological variables, k is the Boltzmann constant, p is the atmospheric pressure, T is the atmospheric temperature, $\Delta\sigma$ is the differential absorption cross-section at on-line and off-line wavelength, $X_{\mathrm{H_2O}}$ is the dry air water vapor mixing ratio, and var is the variance. The pressure, temperature and relative humidity at the origin bin are measured by in-situ sensors placed inside the coherent DIAL. Besides, the meteorological data are also collected using a meteorological tower 2 km away from the DIAL. The absorption cross-section $\Delta\sigma$ and water vapor mixing ratio $X_{\mathrm{H_2O}}$ are corrected for temperature and pressure dependence. For vertically oriented detection, $\Delta\sigma$ and $X_{\mathrm{H_2O}}$ along the bins are calculated using the 1976 US standard atmospheric model with the surface values measured. For horizontally oriented detection, the variations of pressure, temperature and relative humidity are small. Thus $\Delta\sigma$ and $X_{\mathrm{H_2O}}$ at each bin are estimated by meteorological data from DIAL and the meteorological tower. Table 1 summarizes the system and experiment parameters.

Optics EXPRESS

3. Atmospheric measurement results

The atmospheric measurement experiment is conducted in Jinan, Shandong, China (36°49′N, 117°29′E) in June 2023. The location is in a village surrounded by farmlands and buildings, and there is a Taohuashan industrial park in its southwest direction. The heights of the surrounding buildings are relatively low. As shown in Fig. 2, the coherent CO_2 DIAL is placed on the roof of a building with a height of 20 m, which can realize a hemispheric scan with the rotatable platform. A meteorological tower equipped with an in-situ sensor (CRDS, Picarro G2401) is 2 km far away from the coherent DIAL. The in-situ sensor is placed at a height of 50 m above the tower. The plan position indicator (PPI) scanning with an azimuth range of 209°-239° is performed, taking the meteorological tower as the center angle. The vertical detection is conducted for vertical CO_2 and wind measurements. Besides, the velocity azimuth display (VAD) scanning is applied every half hour to measure the 3-D wind fields (including horizontal wind speed, wind direction and vertical speed) instead of just the radial velocity. The 1-s CNR (1×10^4 pulses accumulated) is averaged for wind measurement while 1-min (6×10^5 pulses accumulated) CNR needs to be accumulated for the best compromise to measure CO_2 concentration. The maximum horizontal detection distance is 6 km and the maximum vertical detection distance is over 2 km. The range resolutions of CO_2 concentration and wind fields are both 120 m.

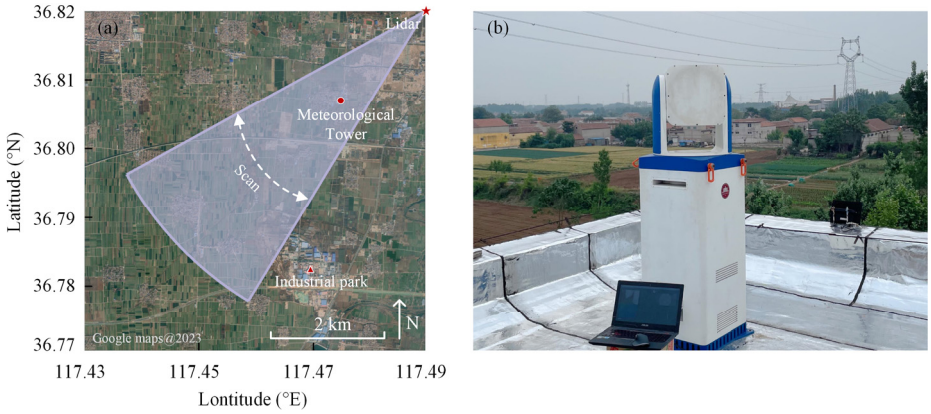

Fig. 2. (a) The experiment site and scanning diagram of the CO_2 coherent DIAL with map overlaid. (b) Picture of the CO_2 coherent DIAL.

3.1. CNR performance

A typical 1-min CNR of horizontal measurement is displayed in Fig. 3(a). In the beginning, both CNR_{on} and CNR_{off} are 5 dB, and then drop to -16 dB and -12 dB respectively at a range of 6 km. According to Eqs. (2)-(6), the retrieval error of CO_2 concentration increases dramatically with range. Figure 3(b) shows Allan deviation of concentration calculated theoretically according to CNR. The trends of significantly decreased error at 120 m and 2100 m are presented as two diagonal lines, with the slope closing to -1/2 in the log scale. For 1 min average times, the retrieval errors of concentration are close to 9.1 ppm at 120 m and 11.2 ppm at 2100 m. After 6 min and 4 min average, the errors at two ranges reach the minimum value of 3.5 ppm and 5.7 ppm, respectively. Refractive turbulence effects on the CNR of coherent detection have been demonstrated [37,38], which is the main factor accounting for the slight error difference between the two ranges. Besides, the upward turn of Allan deviations after 300 s results in non-overlapping with the -1/2 slope, which is probably related to the natural changes in CO_2 concentration caused by turbulence during the measurement period [39].

Optics EXPRESS

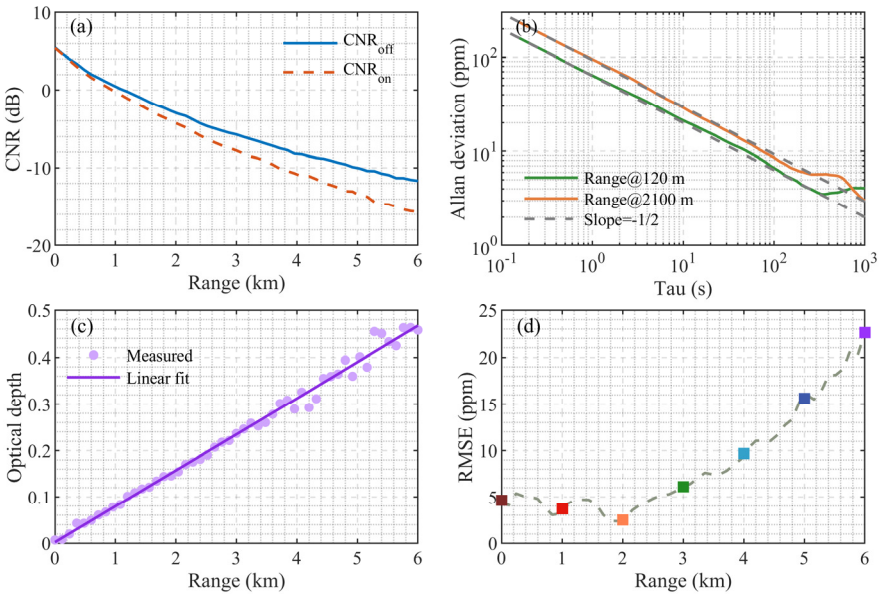

Fig. 3. (a) On-line and off-line CNR in dB for horizontal detection of CO_2 coherent DIAL system. (b) Allan deviations of CO_2 obtained by coherent DIAL. (c) Experimental and linear fitting CO_2 optical depth as a function of range. (d) The RMSE of the 1-min averaged standard deviation of CO_2 at different ranges.

Meanwhile, in Fig. 3(a), both backscatter signals show fluctuations due to the influence of speckle and atmospheric turbulence. For DIAL, the fluctuations of on-line and off-line signals are considered to have a certain degree of consistency, which can be corrected to some extent by calculating the optical depth (OD = -0.5·ln(P_{on}/P_{off})) using two signals. Figure 3(c) shows the 1-min averaged OD, which is also defined as the absorption coefficient multiplied by range. The fluctuation of OD is mainly caused by both natural changes in CO_2 concentration along the range and atmospheric instability. The average CO_2 concentration of 0-6 km is obtained by a mean-square fitting method. Due to the relative uniformity of CO_2 in the horizontal direction, the offset between the measured and the fitted OD also reflects the value of measurement error. The offset increases obviously when the range exceeds 3.5 km, which is consistent with the theoretical error mentioned above. For further analysis, the root-mean-square error (RMSE) is calculated and depicted in Fig. 3(d). Unlike Allan deviation that is based on CNR over 15 min time scales, the RMSE characterizes the uncertainty for each 1 min interval. Allan deviation includes the contribution of CO_2 fluctuations over time, therefore its value is larger than the RMSE. Specifically, the RMSE is 4.6 ppm at the first range bin and reaches 22 ppm at the last range bin of 6 km.

3.2. *In-situ validation*

A comparison between the coherent DIAL and the tower-based in-situ sensor is conducted within a week from 1 June to 7 June 2023 to verify the performance and accuracy of the measurement results. The laser beam is emitted horizontally using PPI scanning shown in Fig. 2(a), and the elevation angle of 2° in order to match the height of the DIAL beam and the in-situ sensor on the tower. The time resolution of the in-situ sensor is 1 s, and the time interval is 1 min for CO_2 measurement. Since the range resolution of CO_2 concentration measured by DIAL is 120 m and the distance between the in-situ sensor and the DIAL is 2 km, the PPI scanning column average concentration along the range of 1920 to 2040 m is used for comparison.

Optics EXPRESS

As shown in Fig. 4, the temporal variations of the CO_2 concentration measured by DIAL agree with that measured by the in-situ sensor during the whole observation period. The DIAL retrieval precision at 2 km is estimated and displayed as shadows. The data obtained from both instruments show that the CO_2 concentration generally decreases during the daytime and increases during the nighttime, which conforms to the common diurnal variation characteristics. That is, the concentration increases at night because of the stable boundary layer and respiration, while it decreases due to the vertical mixing layer and photosynthesis during the day. Nonetheless, the sampling volumes measured by the two instruments are spatially different, and the variation of CO_2 concentration differs day by day due to the influence of external or local sources. The consistency between DIAL and the in-situ sensor also varies.

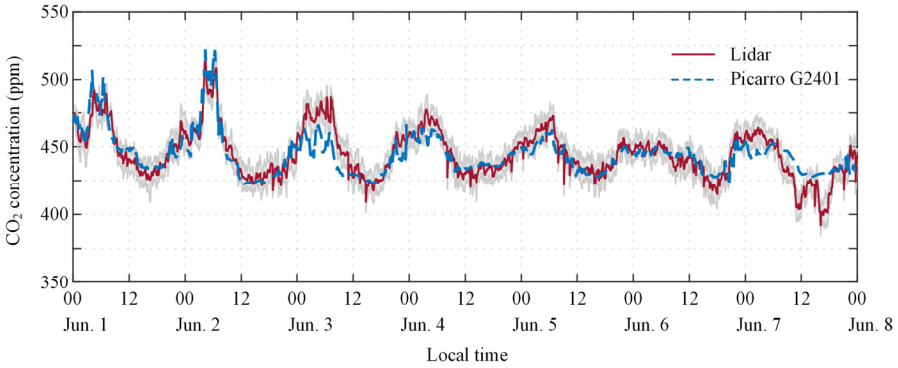

Fig. 4. Comparison of the CO_2 concentration measured by coherent DIAL and in-situ sensor (Picarro G2401) from 1 June to 7 June. The CO_2 concentration of DIAL is made with the column averaged data from 1920 to 2040 m. The retrieval precision is represented as shadows. The data acquisition time for DIAL and the in-situ sensor is 1 min and 1 s, respectively.

Figure 5 and Fig. 6 show the specific statistical difference and correlation analysis between coherent DIAL and the in-situ sensor. The comparison result on 7 June is not further analyzed, due to poor retrieval precision caused by strong turbulence and uneven spatial distribution of CO_2 (See Fig. 9 (a) and (c) for details). Due to the low CNR on 3 June, the detection range and retrieval precision of CO_2 concentration are limited. Thus, the mean and standard deviation of the difference shown in Fig. 5(c) are the largest on the same day with the values of 9.97 ppm and 9.57 ppm, respectively.

Figure 6(c) shows that the concentration of DIAL and the in-situ sensor on the day are highly correlated with a correlation coefficient of 0.92. It indicates that the ability of coherent DIAL to capture changes in CO_2 concentration is not affected by the low retrieval precision. Besides, the mean of difference is small on 6 June with a value of -0.33 ppm, with a negative sign representing a smaller measurement of DIAL than the in-situ sensor. Meanwhile, Fig. 6(f) presents the worst correlation with a correlation coefficient of 0.81 but a low RMSE of 4.44 ppm. The main reason is that the concentration changes gently during most of the time on 6 June. Thus the measurement uncertainties contained in concentration variation affect the correlation between the two instruments. As a whole, the mean and standard deviation of difference from 1 June to 6 June are 2.05 ppm and 7.18 ppm. While the correlation coefficient and RMSE are 0.91 and 5.24 ppm. The results are within an acceptable range that verifies the reliability of coherent DIAL measurement.

Optics EXPRESS

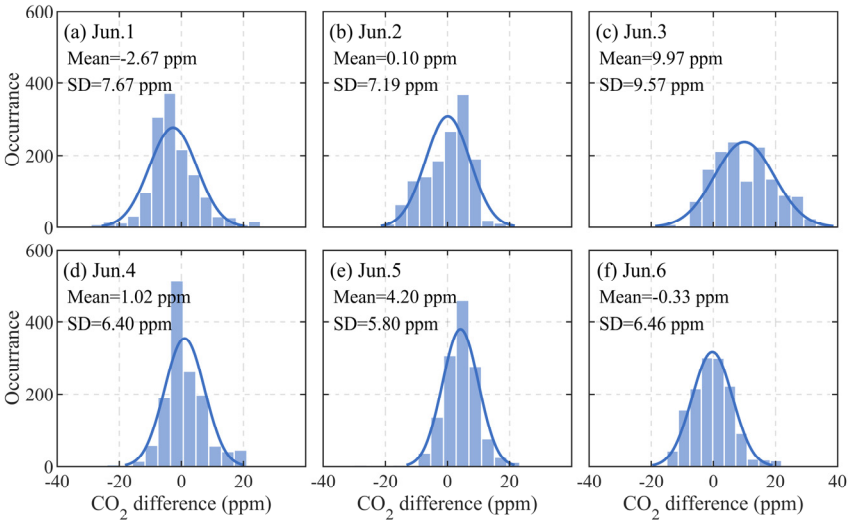

Fig. 5. Statistical analysis of the CO_2 concentration differences between coherent DIAL and the in-situ sensor. The Histogram distributions are displayed day by day for specific analysis. A positive sign of mean difference indicates a larger measurement of DIAL than the in-situ sensor.

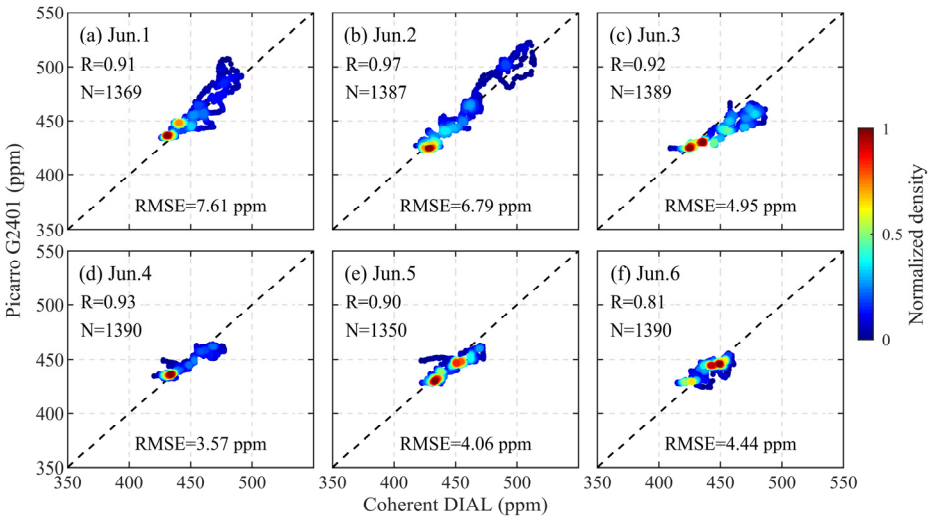

Fig. 6. Scatter diagrams of the CO_2 concentrations measured by coherent DIAL and the in-situ sensor. The color-shaded dots denote normalized density. The dashed lines denote 1:1 lines.

Optics EXPRESS

3.3. Simultaneous CO_2 and wind measurement

Figure 7 illustrates the measurement results using horizontal PPI scanning mode. The 2-D wind fields including wind direction and wind speed are obtained from simultaneously measured radial wind speed. The magnitude of the RMS for wind speed and wind direction is less than 0.6 m/s and 11°, respectively [17]. The negative values indicate being away from the coherent DIAL, while the positive values indicate pointing towards the DIAL. The horizontal wind fields are represented by the wind feather, with a background wind speed of about 2.82 m/s to the southeast. By overlaying the horizontal wind fields onto the range-corrected backscatter signal (PR^2) and the concentration map, the transport process of aerosols and CO_2 can be more clearly observed. The PR^2 is derived from P_{off} and shown in Fig. 7(a), which is relatively weak within a scanning range of 3 km and gets stronger at further ranges. Figure 7(b) shows the CO_2 concentration retrieved according to Eq. (5). Overall, the distribution of concentration is uniform with a background value of 463 ppm. Specifically, the concentrations beyond the 3 km scope are higher than those at close ranges. And the CO_2 concentration is obviously high in the area with a scanning azimuth angle range of 216-224° and a distance range of 5-6 km. It can be seen that the area is adjacent to the industrial park, and the orientation of the industrial park relative to the area is consistent with the wind direction. Thus, the high concentration in the area is inferred as being transmitted from the industrial park.

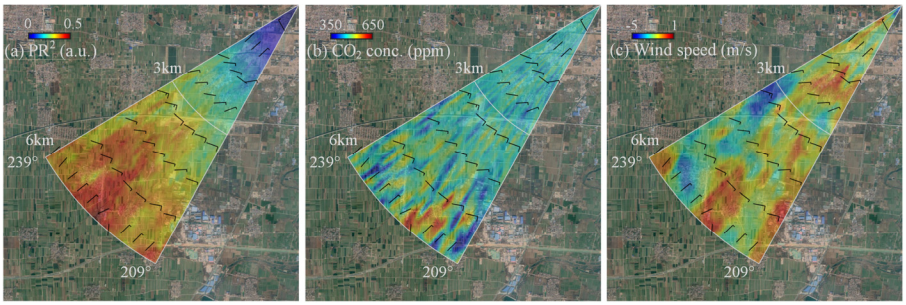

Fig. 7. The horizontal measurement results of coherent DIAL using PPI scanning mode for 00:38, 12 June 2023. (a) Range-corrected backscatter signal (PR^2). (b) CO_2 concentration. (c) Wind field. The wind speed and wind direction are represented by feather symbols and overlaid on PR^2 and concentration maps.

The vertical detection mode is applied for CO_2 and wind speed profile measurement. Figure 8(a), (d) and (g) show the CNRs measurement results at three different times. According to the local meteorological monitoring data, the three cases correspond to around midday, sunset and darkness, respectively. Compared to horizontal detection, the CNRs of vertical detection decrease faster. The CNRs at the origin bin for three cases are less than 0 dB. Then, the values of CNR_{off} drop to -2.6 dB, -6.7 dB and -10 dB at a height of 2 km, respectively. Specifically, the CNRs rapidly decrease after altitude exceeds about 2 km under the influence of the boundary layer. Low boundary layer height (BLH) limits the maximum detectable height. Besides, the fluctuations of CNR are greater than that of the horizontal case due to the influence of clouds. Low CNR and large fluctuation lead to increased errors in concentration inversion.

Figure 8(b), (e) and (h) show the CO_2 concentration profile. The concentrations follow the trend of gradually decreasing with height. Usually, the BLH during the day is higher than that at night due to its stronger turbulence. Thus the maximum detectable heights exceed 2 km at midday and sunset, while the detectable height is lower at darkness. Meanwhile, the concentration measurement errors are represented by the error bar. The heterodyne efficiency and natural changes in atmospheric conditions like refractive index turbulence impact the CNR, especially

Optics EXPRESS

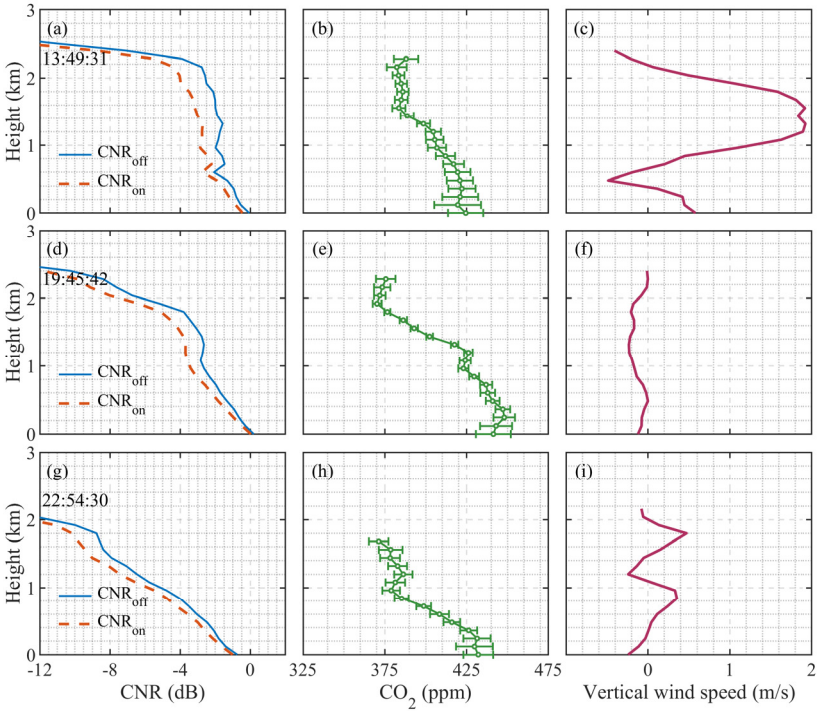

Fig. 8. The vertical measurement results of coherent DIAL for 21 June 2023. (a) CNR, (b) CO_2 concentration profile, (c) wind speed profile at 13:49 (after midday). (d-f) are at 19:45 (near sunset). (g-i) are at 22:54 (after darkness). The error bars of CO_2 concentration are ±1 standard deviation.

with greater impact when the measurement is close to the ground [32,40]. Thus, the concentration errors are higher in the near-field. The first two cases are still during the daytime. Hence, the errors have the characteristics of decreasing first and then increasing within the detectable height range. The minimum error values are 3.3 ppm, 1.9 ppm, and 4.3 ppm, respectively. The higher errors at midday and darkness are mainly caused by strong atmospheric turbulence and low backscattering signals, respectively. Besides, the error at the near ground for midday is larger than in other cases. The possible reason is also related to the decrease in correlation between CNR_{on} and CNR_{off} caused by stronger turbulence during the day.

Figure 8(c), (f) and (i) show the vertical wind speed profile with a mean accuracy of 0.2 m/s [17]. The wind speeds at midday have both positive and negative values with a maximum value of 1.92 m/s, indicating relatively strong turbulence at this time. Thus, the CO_2 concentration is mixed evenly in the vertical direction. For the other two cases, the mean wind speeds of 0-2 km are 0.13 m/s and 0.07 m/s, which corresponds to a stable atmospheric state. The variations of CO_2 concentrations in the vertical direction are greater than that of the first case. Another characteristic of CO_2 is that the near-ground concentration is lower at midday than at sunset and darkness, with concentration values of 424 ppm, 441 ppm and 432 ppm, respectively. The values are negatively correlated with the turbulence intensity, while the turbulence intensity is positively correlated with and is inferred from the variance of vertical wind speed.

Through the above analysis, it can be found that turbulence variations not only play an important role in concentration errors but also affect the distribution of CO_2 concentration. The horizontal transport and vertical mixing process of CO_2 is further specified by combining the CNR and 3-D wind fields obtained by VAD scanning. The standard deviations of horizontal wind speed

Optics EXPRESS

and wind direction are 0.89 m/s and 9.2°, respectively [17]. Figure 9 shows the measurement results. The data amount of CNR and wind fields is less than that of CO_2 concentration due to a half-hour scanning interval of VAD. The maximum detection ranges of the wind fields and CO_2 are limited by the atmospheric boundary layer and atmospheric conditions. An appropriate threshold of backscatter signal is set to reject low CNR data to ensure the retrieval precision.

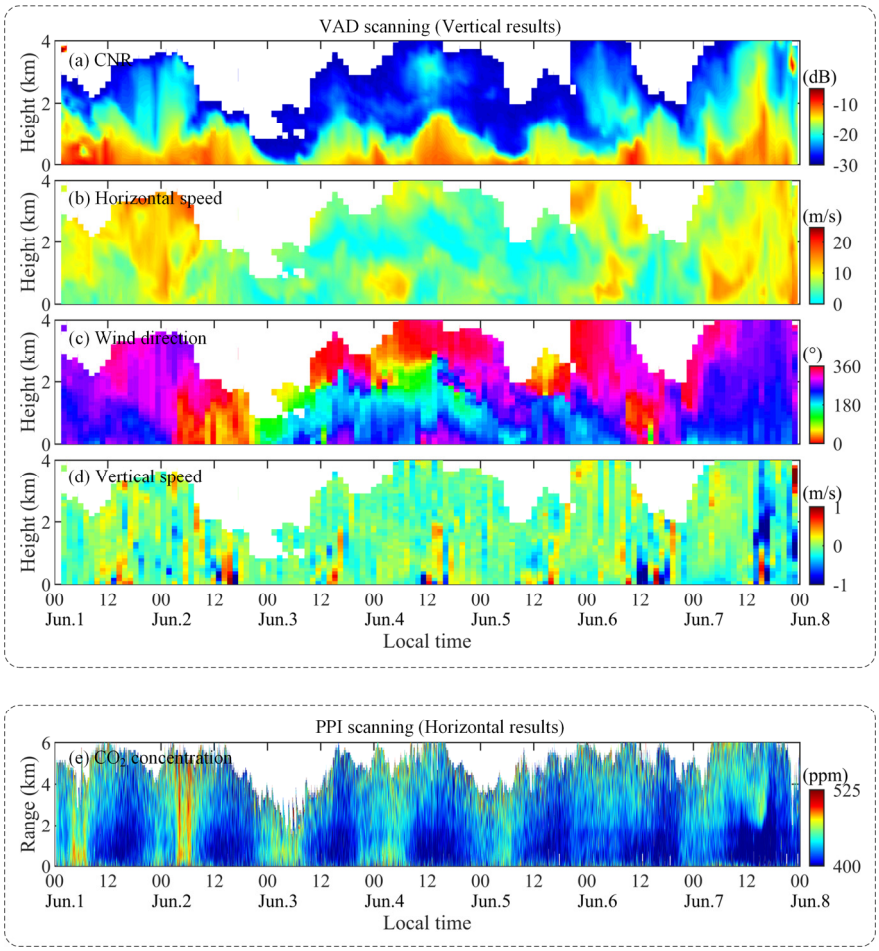

Fig. 9. Continuous observation results of CO_2 coherent DIAL from 1 June to 7 June 2023. (a) CNR, (b) Horizontal wind speed, (c) Horizontal wind direction, (d) Vertical wind speed using VAD scanning mode every half hour. (e) CO_2 concentration per minute interval for horizontal measurement. Negative vertical wind speed denotes rising wind.

The horizontal wind speed near the ground is the smallest on 3 June and the largest on 7 June, with an average speed of 3.5 m/s and 9.5 m/s, respectively. The wind direction near the ground varies with time, mainly dominated by westerly winds. Meanwhile, the vertical wind speed represents the vertical component of turbulence kinetic energy. The BLH increases as turbulence intensity becomes stronger. During the observation period, the BLH generally begins to rise at 8:00 and reaches the maximum value at 14:00. Figure 9(c) and (d) show a significant negative correlation between the BLH and the CO_2 concentration. Obviously, the relatively high BLH and large horizontal wind speed on June 7 accelerate the horizontal and vertical diffusion of CO_2, resulting in low CO_2 concentrations. However, the exception occurs on 2 June, the BLH rises at 03:00 while the CO_2 concentration increases rapidly over the entire range. Meanwhile,

Optics EXPRESS

the horizontal wind speeds at high altitudes are larger than 10 m/s with a wind direction of northwest within the corresponding time period. And the upper atmosphere reaches the ground under the influence of relatively strong turbulence kinetic energy. It can be inferred that the transport of external anthropogenic emissions from the northwest rather than local accumulation results in an increase in CO_2 concentration on 2 June. On the other hand, Fig. 9(b) and (e) show that CO_2 exhibits significant spatial distribution characteristics when the horizontal wind speeds near the ground are high. Namely, the concentrations are higher at long ranges than at near ranges. Considering that the Taohuashan industrial park is located in the far-field of DIAL, the phenomenon is mainly caused by the horizontal transmission of local emissions. Specifically, both the horizontal wind speed and turbulence intensity are strong during the day on 7 June, making the daytime concentration at near ranges lower than on other days. And with the development of time, the concentration is gradually mixed evenly over the whole range.

4. Conclusion

A coherent DIAL has been demonstrated to measure 3-D CO_2 and wind fields. The wavelength of 1.57 µm is applied to the coherent lidar regardless of the weak absorption line intensity. Besides, the performance of the coherent DIAL is conducted using a tower-based CRDS through a-week consecutive observation. The comparison between the two instruments shows good agreement with a mean and standard deviation of 2.05 ppm and 7.18 ppm, while the correlation coefficient and RMSE are 0.91 and 5.24 ppm, respectively. The regional distributions of CO_2 and 2-D wind fields are measured through PPI scanning. And the 3-D wind fields are obtained through VAD scanning. Besides, the experiment is also conducted by looking vertically for CO_2 profile measurement. The maximum detection range of horizontal measurement is 6 km while that of vertical measurement is 2 km. The range resolution of CO_2 concentration and wind fields are both 120 m, while the time resolutions are 1 min and 1 s, respectively. The results show the vertical mixing process of CO_2 concentration under the influence of turbulence, and the horizontal transport process under the influence of horizontal wind speed and direction. The specific contributions of external and local emission sources to the distribution of CO_2 concentration are clarified. In fact, the measurement of the in-situ sensor represents an average concentration of an effective area called footprint, which is mainly determined by horizontal wind and turbulence [41,42]. In the future, the comparison results between DIAL and the in-situ sensor can be further improved by sampling CO_2 within different regions to match the footprint.

Appendix: intensity estimation and comparison

The direct detection converts the incoming photon flux to a measurable signal current by means of an amplification process. The signal intensity is linearly related to the baseband photocurrent. Increasing the SNR of direct detection systems requires high pulse energy or detector quantum efficiency, while using single-photon detection is not limited by this noise problem [43]. However, the detector current of the single-photon direct system is prone to saturation in the near-field. In contrast to the direct detection systems, the coherent detection uses a diffraction-limited system which allows only one speckle cell imaged onto the detector surface. The signal intensity is related to the square of the intermediate frequency (IF) photocurrent envelope. The coherent detection is almost unaffected by solar background noise, and the radiometric sensitivity of coherent detection is approximately 2-3 orders of magnitude higher than that of direct detection combining ordinary detectors. It means that the coherent detection allows smaller systems to satisfy the same range requirements when its sensitivity is comparable to the direct detection. In other words, coherent detection increases maximum range capability with similar size systems.

The coherent detection signal $i(t)$ contains IF signal photocurrent $i_s(t)$ and noise photocurrent $i_n(t)$, which is described as [44]

$$i(t) = i_s(t) + i_n(t). \tag{7}$$

Optics EXPRESS

The CNR is defined as the ratio of the signal power and the noise power, reflecting the strength of the backscatter signal, which is expressed by

$$CNR = \left\langle i_s(t)^2 / i_n(t)^2 \right\rangle, \tag{8}$$

where $\langle\ \rangle$ represents ensemble average. The signal power can be estimated from the area of the signal spectrum using one-peak Gaussian fitting method. Then the CNR is further obtained. The Gaussian model is described as

$$S(f) = I \exp[-(f - f_a)^2/(2\sigma^2)], \tag{9}$$

where f is the mean Doppler frequency shift from aerosols, I is the peak intensity, σ is the spectrum width. The above parameters and the area of the power spectrum are determined using a least squares fitting.

As mentioned above, the dynamic range of direct detection is limited, which is reflected in occurring nonlinear effect for strong near-field signals. The nonlinear effect affects the ratio of signal intensity between on-line and off-line, resulting in errors in concentration retrieval. In order to evaluate the signal power estimated by Gaussian fitting and the detection sensitivities of the coherent system, a comparison experiment with the SNSPD-based direct system is conducted.

As shown in Fig. 10, the emission of a continuous wave (CW) laser is divided into two portions: one portion is attenuated by a variable attenuator, while the other portion is used as a local oscillator. Then, the attenuated light passes through an in-line polarizer and is further divided into two parts: one part enters a single-mode (non-polarization-maintaining) SNSPD for direct detection, and the other part is mixed with the local oscillator for coherent detection. The beat signal is generated by focusing both signals into a BD with its intensity estimated using Gaussian fitting. For ease of reference, the optical power input to the two detectors is converted into the photon counts per second. According to the lidar equation, the backscatter signal that passes through the atmosphere attenuates proportionately with the range squared.

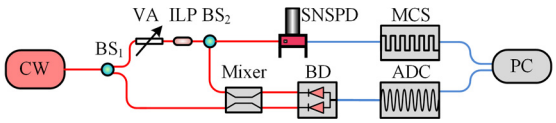

Fig. 10. System setup for comparison. CW, continuous wave laser; BS, beam splitter; VA, variable attenuator; ILP, In-polarizer; SNSPD, superconducting nanowire single photon detector; MCS, multi-channel scaler.

Figure 10(a) shows the noise-corrected and normalized power spectrum density of coherent signal. The signal power is determined using the Gaussian fitting area. Fig. 11(b) shows the output counts of SNSPD and the calculated power intensity of BD. The left axis indicates direct detection while the right axis indicates coherent detection. The input count rate range of SNSPD is set to within 150 MHz while that of BD is set to over 450 MHz. The response of the direct detection is almost linear within a certain input count range with a determination coefficient (R^2) of 1, and begins to show nonlinearity when the input count rate exceeds 90 MHz. It means that the performance of direct detection is expected better at lower input counts. For coherent detection, the response appears to be linear at higher input counts. The R^2 for linear fitting is 1, which experimentally verifies the linear response of coherent detection.

Although the inversion error increases due to the decreased sensitivity of coherent detection to weak signals, the coherent detection signals intensity estimated from Gaussian fitting response linearly during the experiment. Therefore, the inverted absolute concentration of atmospheric CO_2 is ensured in the experiment. However, the noise process and signal extraction method from weak signals in coherent detection is the remaining issue. In the future, the response

Optics EXPRESS

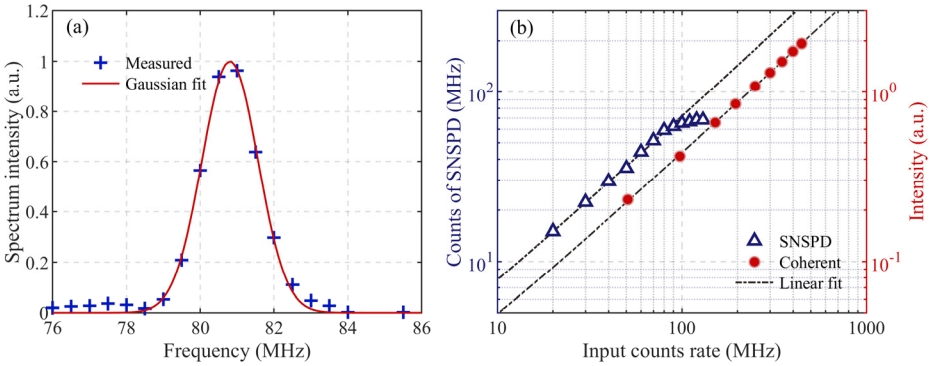

Fig. 11. (a) An example of noise-corrected and normalized power spectrum density at the first range bin, measured at 09:48 on 26 March 2023. (b) Linearity verification of coherent detection by comparing with direct detection. The left axis indicates direct detection while the right axis indicates coherent detection.

characteristics of coherent detection under weak signals need further research to improve its concentration inversion capability for a larger dynamic range.

Funding. National Key Research and Development Program of China (2022YFF0606400); National Natural Science Foundation of China (42305147); Natural Science Foundation of Jiangsu Province (BK20230428).

Disclosures. The authors declare that there are no conflicts of interest related to this article.

Data availability. Data underlying the results presented in this paper are not publicly available at this time but may be obtained from the authors upon reasonable request.

References

1. V. Masson-Delmotte, P. Zhai, A. Pirani, *et al.*, eds., "Climate Change 2021: The physical science basis," in *Contribution of Working Group I to the Sixth Assessment Report of the Intergovernmental Panel on Climate Change (IPCC)* (Cambridge University, 2021).
2. M. Zou, X. Xiong, Z. Wu, *et al.*, "Increase of Atmospheric Methane Observed from Space-Borne and Ground-Based Measurements," Remote Sens. **11**(8), 964 (2019).
3. W. Wang, W. Xiao, C. Cao, *et al.*, "Temporal and spatial variations in radiation and energy balance across a large freshwater lake in China," J. Hydrol. (Amsterdam, Neth.) **511**, 811–824 (2014).
4. Z. Wu, A. Vermeulen, Y. Sawa, *et al.*, "Investigating the differences in calculating global mean surface CO_2 abundance: the impact of analysis methodologies and site selection," Atmos. Chem. Phys. **24**(2), 1249–1264 (2024).
5. S. Fang, P. P. Tans, B. Yao, *et al.*, "Study of atmospheric CO_2 and CH_4 at Longfengshan WMO/GAW regional station: The variations, trends, influence of local sources/sinks, and transport," Sci. China Earth Sci. **60**(10), 1886–1895 (2017).
6. C. D. Keeling, R. B. Bacastow, A. E. Bainbridge, *et al.*, "Atmospheric carbon dioxide variations at Mauna Loa Observatory, Hawaii," Tellus **28**(6), 538–551 (1976).
7. I. C. Prentice, G. D. Farquhar, M. J. R. Fasham, *et al.*, The carbon cycle and atmospheric carbon dioxide, in *Climate Change 2001: the Scientific Basis: Contribution of Working Group I to the Third Assessment Report of the Intergovernmental Panel on Climate Change* (Cambridge Univ. Press, 2001), pp. 185–237.
8. E. Cadiou, D. Mammez, J.-B. Dherbecourt, *et al.*, "Atmospheric boundary layer CO_2 remote sensing with a direct detection LIDAR instrument based on a widely tunable optical parametric source," Opt. Lett. **42**(20), 4044–4047 (2017).
9. G. Han, W. Gong, H. Lin, *et al.*, "Study on Influences of Atmospheric Factors on Vertical CO_2 Profile Retrieving From Ground-Based DIAL at 1.6 μm," IEEE Trans. Geosci. Remote Sensing **53**(6), 3221–3234 (2015).
10. Y. Shibata, C. Nagasawa, and M. Abo, "Development of 16 μm DIAL using an OPG/OPA transmitter for measuring atmospheric CO_2 concentration profiles," Appl. Opt. **56**(4), 1194–1201 (2017).
11. L. Fiorani, S. Santoro, S. Parracino, *et al.*, "Volcanic CO_2 detection with a DFM/OPA-based lidar," Opt. Lett. **40**(6), 1034–1036 (2015).
12. S. Yu, Z. Zhang, M. Li, *et al.*, "Multi-frequency differential absorption lidar incorporating a comb-referenced scanning laser for gas spectrum analysis," Opt. Express **29**(9), 12984–13995 (2021).
13. S. Yu, Z. Zhang, H. Xia, *et al.*, "Photon-counting distributed free-space spectroscopy," Light: Sci. Appl. **10**(1), 212 (2021).

Optics EXPRESS

14. B. J. Rye and R. M. Hardesty, "Estimate optimization parameters for incoherent backscatter heterodyne lidar," Appl. Opt. **36**(36), 9425–9436 (1997).
15. J. Bösenberg, "Ground-based differential absorption lidar for water-vapor and temperature profiling: methodology," Appl. Opt. **37**(18), 3845–3860 (1998).
16. G. Ehret, C. Kiemle, M. Wirth, *et al.*, "Space-borne remote sensing of CO_2, CH_4, and N_2O by integrated path differential absorption lidar: a sensitivity analysis," Appl. Phys. B **90**(3-4), 593–608 (2008).
17. J. Yuan, Y. Wu, Z. Shu, *et al.*, "Real-Time Synchronous 3-D Detection of Air Pollution and Wind Using a Solo Coherent Doppler Wind Lidar," Remote Sens. **14**(12), 2809 (2022).
18. D. Tang, T. Wei, J. Yuan, *et al.*, "Observation of bioaerosol transport using wideband integrated bioaerosol sensor and coherent Doppler lidar," Atmos. Meas. Tech. **15**(9), 2819–2838 (2022).
19. F. Gibert, G. J. Koch, J. Y. Beyon, *et al.*, "Can CO_2 Turbulent Flux Be Measured by Lidar? A Preliminary Study," J. Atmos. Ocean. Tech. **28**(3), 365–377 (2011).
20. J. Zhao, M. Zhang, W. Xiao, *et al.*, "An evaluation of the flux-gradient and the eddy covariance method to measure CH_4, CO_2, and H_2O fluxes from small ponds," Agr. Forest Meteorol. **275**, 255–264 (2019).
21. C. Lin, J. B. Cohen, S. Wang, *et al.*, "A new perspective on the spatial, temporal, and vertical distribution of biomass burning: quantifying a significant increase in CO emissions," Environ. Res. Lett. **15**(10), 104091 (2020).
22. R. M. Hardesty, "Coherent DIAL measurement of range-resolved water vapor concentration," Appl. Opt. **23**(15), 2545–2553 (1984).
23. C. J. Karlsson, FÅA Olsson, D. Letalick, *et al.*, "All-fiber multifunction continuous-wave coherent laser radar at 1.55 µm for range, speed, vibration, and wind measurements," Appl. Opt. **39**(21), 3716–3726 (2000).
24. S. Kameyama, T. Ando, K. Asaka, *et al.*, "Compact all-fiber pulsed coherent Doppler lidar system for wind sensing," Appl. Opt. **46**(11), 1953–1962 (2007).
25. L. Lombard, M. Valla, C. Planchat, *et al.*, "Eyesafe coherent detection wind lidar based on a beam-combined pulsed laser source," Opt. Lett. **40**(6), 1030–1033 (2015).
26. H. Xia, G. Shentu, M. Shangguan, *et al.*, "Long-range micro-pulse aerosol lidar at 1.5 µm with an upconversion single-photon detector," Opt. Lett. **40**(7), 1579–1582 (2015).
27. M. Imaki, H. Tanaka, K. Hirosawa, *et al.*, "Demonstration of the 1.53-µm coherent DIAL for simultaneous profiling of water vapor density and wind speed," Opt. Express **28**(18), 27078–27096 (2020).
28. N. Cezard, S. Le Mehaute, J. Le Gouët, *et al.*, "Performance assessment of a coherent DIAL-Doppler fiber lidar at 1645 nm for remote sensing of methane and wind," Opt. Express **28**(15), 22345–22357 (2020).
29. G. J. Koch, B. W. Barnes, M. Petros, *et al.*, "Coherent differential absorption lidar measurements of CO_2," Appl. Opt. **43**(26), 5092–5099 (2004).
30. F. Gibert, P. H. Flamant, D. Bruneau, *et al.*, "Two-micrometer heterodyne differential absorption lidar measurements of the atmospheric CO_2 mixing ratio in the boundary layer," Appl. Opt. **45**(18), 4448–4458 (2006).
31. S. Ishii, K. Mizutani, H. Fukuoka, *et al.*, "Coherent 2 µm differential absorption and wind lidar with conductively cooled laser and two-axis scanning device," Appl. Opt. **49**(10), 1809–1817 (2010).
32. F. Gibert, D. Edouart, C. Cénac, *et al.*, "2-µm Ho emitter-based coherent DIAL for CO_2 profiling in the atmosphere," Opt. Lett. **40**(13), 3093–3096 (2015).
33. J. Lahyani, J. Le Gouët, F. Gibert, *et al.*, "2.05-µm all-fiber laser source designed for CO_2 and wind coherent lidar measurement," Appl. Opt. **60**(15), C12–C19 (2021).
34. T. Wei, H. Xia, Y. Wu, *et al.*, "Inversion probability enhancement of all-fiber CDWL by noise modeling and robust fitting," Opt. Express **28**(20), 29662–29675 (2020).
35. B. J. Rye and R. M. Hardesty, "Discrete spectral peak estimation in incoherent backscatter heterodyne lidar. I. Spectral accumulation and the Cramer-Rao lower bound," IEEE Trans. Geosci. Remote Sensing **31**(1), 16–27 (1993).
36. I. E. Gordon, L. S. Rothman, R. J. Hargreaves, *et al.*, "The HITRAN2020 molecular spectroscopic database," J. Quant. Spectrosc. Radiat. Transfer **277**(277), 107949 (2022).
37. N. Menyuk and D. K. Killinger, "Temporal correlation measurements of pulsed dual CO_2 lidar returns," Opt. Lett. **6**(6), 301–303 (1981).
38. D. K. Killinger and N. Menyuk, "Effect of turbulence-induced correlation on laser remote sensing error," Appl. Phys. Lett. **38**(12), 968–970 (1981).
39. G. A. Wagner and D. F. Plusquellic, "Multi-frequency differential absorption LIDAR system for remote sensing of CO_2 and H_2O near 1.6 µm," Opt. Express **26**(15), 19420–19434 (2018).
40. A. Belmonte, "Coherent return turbulent fluctuations in ground lidar systems profiling along slant paths," Opt. Express **13**(23), 9598–9604 (2005).
41. N. Kljun, P. Calanca, M. W. Rotach, *et al.*, "A simple two-dimensional parameterisation for Flux Footprint Prediction (FFP)," Geosci. Model Dev. **8**(11), 3695–3713 (2015).
42. Z. Gao, L. Bian, and X. Zhou, "Measurements of turbulent transfer in the near-surface layer over a rice paddy in China," J. Geophys. Res. **108**(D13), 2002JD002779 (2003).
43. M. Shangguan, Y. Guo, Z. Liao, *et al.*, "Sensing profiles of the volume scattering function at 180° using a single-photon oceanic fluorescence lidar," Opt. Express **31**(24), 40393–40410 (2023).
44. P. Gatt and S. W. Henderson, "Laser Radar Detection Statistics: A Comparison of Coherent and Direct Detection Receivers," Proc. SPIE **4377**(3), 251–262 (2001).